Chemical Engineering Journal 497 (2024) 154407

Contents lists available at ScienceDirect

Chemical Engineering Journal

journal homepage: www.elsevier.com/locate/cej

Interfacially engineered palladium nanoparticle-decorated nickel oxide nanostructured electrocatalysts for high-performance hydrogen evolution reaction

Jeongsik Choi [a,1], Que Thi Nguyen [b,1], Soojin Park [a], Balaji G. Ghule [c], Jong Hyun Park [d], Jae Ryang Park [d], Umesh T. Nakate [e,*], Ji-Hyun Jang [c], Dong-Won Kim [e], Sungjune Park [b,*]

[a] Department of Nano Convergence Engineering, Jeonbuk National University, Jeonju 54896, Republic of Korea
[b] School of Chemical Engineering, Sungkyunkwan University, Suwon 16419, Republic of Korea
[c] School of Energy and Chemical Engineering, Ulsan National Institute of Science and Technology, Ulsan 44919, Republic of Korea
[d] Materials Science and Chemical Engineering Center, Institute for Advanced Engineering, Yongin 17180, Republic of Korea
[e] Department of Chemical Engineering, Hanyang University, Seoul 04763, Republic of Korea

ARTICLE INFO

Keywords:
Hydrogen evolution reaction (HER)
Water splitting
Electrocatalyst
Pd-decorated NiO nanostructured electrode

ABSTRACT

Water splitting has been known as a promising candidate for electrochemical green hydrogen. The hydrogen evolution reaction (HER), which is the half-reaction for water splitting at the cathode, typically requires a high overpotential (η_{HER}). Transition metal-based nanomaterials (TMBMs) are appealing electrocatalysts for the HER because of their ability to reduce the η_{HER}. Interfacial engineering is an effective strategy for utilizing TMBMs, wherein noble metals are used to create several active sites on the surfaces of nanostructured TMBMs. This approach simultaneously exploits the advantages of the intrinsically high HER performance of noble metals and the large surface area of TMBM nanostructures. In this study, we synthesized nickel oxide (NiO) nanoplates *via* an alkali-free hydrothermal approach to produce highly purified electrodes with large surface area, followed by decoration with palladium (Pd) nanoparticles *via* wet impregnation. Although various combinations of noble metal-decorated TMBMs are available for the HER, Pd and NiO were chosen due to their intrinsically high HER performance and facile processability, respectively. The Pd/NiO electrocatalyst with an ideal compositional threshold of both elements showed outstanding HER performance, affording low η_{HER} of 59 and 92 mV at high current densities of 50 and 100 $mAcm^{-2}$, respectively, and a low Tafel slope of 52 $mVdec^{-1}$. After 50 h of a stability test, 92 % of the initial performance of the Pd/NiO electrode was maintained. These experimental results have been supported by the Gibbs free energy for Pd/NiO and pristine NiO electrocatalysts estimated in the water dissociation using density functional theory (DFT) calculations. This facile approach of alkali-free hydrothermal synthesis and subsequent wet impregnation to synthesize electrocatalysts based on interface engineering can be further utilized to explore high performance green hydrogen production.

1. Introduction

As the energy demand increases owing to population growth and industrialization, the interest in eco-friendly and efficient energy sources for replacing fossil fuels and mitigating air pollution is surging. Hydrogen (H_2) is considered a potential alternative clean energy source because it can be largely produced from water as a byproduct when combusted [1]. Electrolysis of water (EOW) is an economical and efficient method of producing pure H_2 *via* the hydrogen evolution reaction (HER) [2]. However, the high overpotential (theoretically, the overall EOW overpotential requires $\eta_{EOW} \geq 1.23$ V, whereas a value 0.55–0.77 V higher is required practically) must be overcome [3]. Hence, developing novel and efficient electrocatalysts is essential for maximizing the water splitting efficiency by reducing the η_{EOW} for wider applications in the future.

The efficiency of water electrolysis can be promoted through redox reactions on the surface of transition metals owing to the free d-orbital electrons of the metals [4]. Transition metals have been used to create

* Corresponding authors.
E-mail addresses: umesh.nakate@gmail.com (U.T. Nakate), sungjunepark@skku.edu (S. Park).
[1] These authors contributed equally to this work.

https://doi.org/10.1016/j.cej.2024.154407
Received 16 May 2024; Received in revised form 17 July 2024; Accepted 28 July 2024
Available online 9 August 2024

various materials such as phosphides, chalcogenides, carbides, phosphates, oxides, hydroxides, perovskites, and nitrides [5]. Among them, transition metal oxides (TMOs) have been drawn attention because of their exclusive properties, such as low cost, abundance, and structural diversity. Transition metal oxides also offer a number of surface active sites *via* the formation of nanomorphology [6]. NiO nanostructured electrodes have been utilized for the HER due to their high electrocatalytic efficiency and facile transformation to nanostructured morphologies with a large surface area, which can boost HER performance. Zhang *et al.* constructed oxygen vacancies in NiO nanorods by the in-situ cation exchange in the gas phase method and achieved the η_{HER} of 110 mV at 10 mA cm^{-2} [7]. On the contrary, NiO nanoparticles fabricated using the drop-casting method afforded the η of 373 and 268 mV for the OER and HER at 10 mA cm^{-2}, respectively, *via* Ni^{2+}/Ni^{3+} transition-assisted EOW [8]. To fabricate nanostructured electrodes, hydrothermal synthesis is considered as one of the most facile approaches [9]. Although various alkaline-reducing reagents have been used to accelerate the formation the electrodes during the hydrothermal synthesis [10], the byproducts possibly caused impurities, unusual morphologies, and damaged gas thereby requiring extra purifications [11]. Various literatures have successfully fabricated metal oxides *viz.* alkali-free hydrothermal method such as Co_3O_4, SnO_2; implying the high efficiency of alkali-free hydrothermal for nanostructured metal oxide preparation [12,13]. Thus, in this work, the NiO electrodes with uniformly grown nanostructured morphologies is prepared by alkali-free hydrothermal synthesis.

Despite the promising features, NiO electrocatalyst has limited conductivity, which can lower the EOW efficiency [14]. Thus, plenty of interfacial engineering methods, such as single-atom-/heteroatom-doping, core–shell structuring, and hierarchical geometry design, have been studied to expand the EOW efficiency by simultaneously taking advantage of the intrinsic advantages of multiple elements [15–17]. Moreover, the interfacial engineering approach can generate rapid redox reactions by reinforcing the physical properties of the interface layer, which absorbs electrolyte reactants, transfers electrons, and desorbs products [18]. Pristine noble metals are recognized as ideal electrodes for lowering the η_{HER} and establishing stable interfaces with TMOs (*e.g.* NiO, MnO, and CoO) to enhance the HER performance despite their drawbacks in terms of cost and scarcity [19]. Therefore, it is desirable to decorate economically advantageous electrocatalysts substrates with small amounts of noble metals. Various studies have explored this approach, achieving extraordinary results, such as $\eta_{HER} \leq$ 100 mV at a high current density (up to 100 mA cm^{-2}), which is comparable to that of a commercial Pt electrode, where Pt is considered as a superior catalyst for the HER. Yan et al. reported Pt filling into NiO exhibited the η_{HER} of 20 mV at 10 mA/cm^2 [20]. Zhang et al. reported the NiO@Ru for high-efficiency overall water splitting at a voltage of 1.55 V [21]. Barhoum *et al.* reported a composites named CNF-Ni/NiO-Pd displayed a low η_{HER} of 63 mV at 10 mA/cm^2 [22]. Based on these underlying principles, we refined a facile interfacial engineering strategy for decorating the surfaces of nanostructured transition metal oxides with pristine noble metals to produce effective and economical electrocatalysts for HER applications. Compared to various pristine noble metals, the chemical and electronic affinities of palladium (Pd) are similar to those of Pt, making Pd a promising economic substitute for Pt [23]. Moreover, Pd has a high adsorption energy; thus, it can attack reactants in the electrolyte at the interface of the electrode. Hydrogen adsorption on Pd nanoparticles proceeds via two distinct phases depending on the hydrogen concentration as the reaction progresses [24]. The hydrogen-poor solid-state solution (α-phase) exists in the initial reaction and the hydrogen-rich hydride (β phase) appears when a huge amount of hydrogen is generated. Suzana *et al.* indicated that the α–β phase-transformation of hydrogen adsorbed on Pd NPs allows the electrode to adsorb a large amount of hydrogen and accelerates the kinetics of the HER [25].

Thus, in this work, we develop an interfacial engineered electrocatalyst, namely, Pd-decorated NiO nanostructured electrodes, by alkali-free hydrothermal synthesis of NiO nanostructures and subsequent wet impregnation of Pd NPs, for HER applications. NiO with nanoporous morphologies can support the Pd NPs and enhance the redox reactions during the HER owing to the large electrode/electrolyte interfaces. Comparative analysis with other pristine-noble-metal-decorated NiO species (Ag/NiO, Ru/NiO and Au/NiO) shows that Pd/NiO with low amount of Pd (3 mM $PdCl_2$) achieves the highest HER performance, affording η_{HER} of 59 and 92 mV at high current densities of 50 and 100 mAcm^{-2}, respectively, a Tafel slope of 52.05 mV dec^{-1} in 1 M KOH solution, and maintains 92 % efficiency after 50 h of a stability test. The experimental results are supported by theoretical studies, where DFT analysis of the Gibbs free energy and water molecule dissociation energy shows that Pd/NiO (0.52 V) required lower energy than that of NiO (0.78 V) despite the trace amount of Pd NPs (0.5 wt%). This facile approach for producing nanostructured transition metal oxide electrodes decorated with small amounts of noble metals based on interfacial engineering can be further utilized for developing novel and efficient electrocatalysts for the HER.

2. Results and discussion

2.1. Mechanism of Pd/NiO synthesis

Fig. 1 illustrates the mechanism of formation of the NiO nanoplates by alkali-free hydrothermal synthesis. The nickel nitrate salt dissolves in DI water to form Ni^{2+} cations and NO_3^- anions. During hydrothermal synthesis, the DI water may partially dissociate into H^+ and OH^- species.

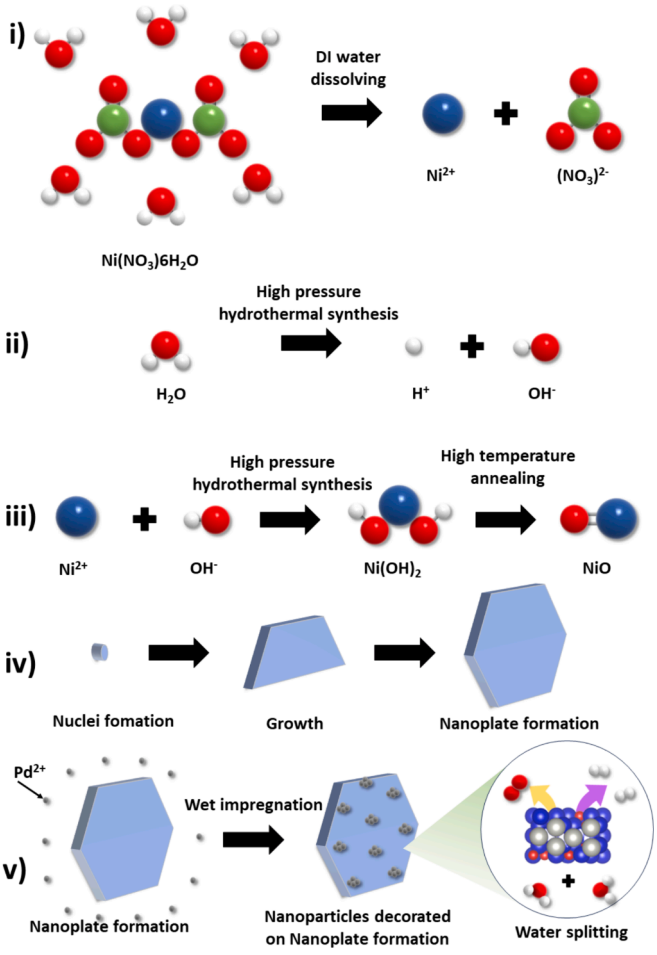

Fig. 1. Schematics showing the mechanism of formation and growth of NiO nanoplate and decoration of Pd nanoparticles on NiO nanoplate.

The Ni^{2+} cations strongly attract and react with the OH^- species to form nickel hydroxide ($Ni(OH)_2$), which is further annealed to form NiO.

The NiO nuclei that were assembled on the surface of the nickel foam (NF) grew slowly to form a 2D structure. The synthesis time, temperature, and concentration of the nickel nitrate precursor solution affected the morphology of the NiO nanoplates. Once the nanostructured NiO was formed, a wet impregnation technique was used to decorate the NiO nanoplates with Pd nanoparticles. In the wet impregnation process, Pd^{2+} and Cl^- ions around the surface of the NiO nanoplates can create a thin cover layer. The mechanism of formation of the Pd NPs on the NiO surface can be explained by the fact that NiO can possibly be converted from Ni^{2+} to Ni^{3+} and can donate electrons to Pd^{2+} at high temperatures, forming Pd^0 which further grows as nanoparticles anchored on the NiO surface.

2.2. Morphological and structural studies of electrocatalysts

To verify the successful fabrication of Pd/NiO electrode by hydrothermal synthesis and subsequent wet impregnation, various morphological and structural characterizations have been studied. Firstly, the atomic force miscroscopy (AFM) were collected to dissect the topography of the Pd-decorated NiO. The 3D AFM topography images of scan area of 5 μm × 5 μm for NF, NiO, and Pd/NiO were obtained as shown in **Fig. S1**, Fig. 2**a and b**, respectively. Compared to the microscopically planar topography of NF, the nanoplate-like structures can be observed for NiO and Pd/NiO samples. The increased surface height of the NiO (781.768 nm) and Pd/NiO (964.381 nm) compared to that of the NF (328.344 nm) indicates the successfully grown active materials on the NF surface. Moreover, the root mean square roughness (R_q) values of NiO (104.916 nm) and Pd/NiO (111.095 nm) is higher than that of the NF (46.322 nm) implying the larger variation in NiO and Pd/NiO due to the nanoporous morphologies [26]. The field-emission scanning electron microscopy (FE-SEM) images show in **Fig. S1 – S3,** Fig. 2**c and d** display a 2D array consisting of numerous homogeneously aligned nanoplates and nanoparticles for Pd/NiO which is clearly different than NF and NiO samples. This morphology may generate a larger surface area and a larger number of exposed active sites at the electrode/electrolyte interface, resulting in increased electrocatalytic activity. The energy dispersive X-ray spectroscopy (EDS) mapping of Pd/NiO shows the dense and uniform presence of Pd, Ni, and O on the NF surface (**Fig. S4**). The transmission electron microscopy (TEM) and high-resolution TEM (HR-TEM) analyses revealed the nanostructures at higher magnification and the planar interlayers of Pd/NiO; the average sized of Pd NPs has been estimated around 10 nm. (Fig. 2**e, f,** and **g**). Selected-area electron diffraction (SAED) analysis confirmed the crystalline nature of Pd/NiO (Fig. 2**h**). The image of 2D Pd/NiO clearly shows the Pd lattice fringe of the (1 1 1) plane with a d-spacing of 0.23 nm and that of the NiO (0 0 3) plane with a d-spacing of 0.25 nm. The regular pattern of bright spots intimates the single-crystalline feature of the NiO and Pd NPs, as confirmed by comparing the SAED pattern and the lattice fringes from the X-ray diffraction analysis (XRD) peaks corresponding to the (1 1 1), (2 0 0), (2 2 0), (2 2 2), (4 0 0), and (3 3 1) planes for Pd and the (0 0 3), (1 1 0), and (0 2 1) planes of NiO, respectively [27,28]. The XRD pattern of Pd/NiO matched well with those of the NiO (JCPD card PDF#22-1189) and Pd (JCPD card PDF#05-0681) structures, as shown in Fig. 2**i**; the background peak (high intensity) originated from the NF substrate (JCPD card PDF#87-0712) [29]. Fig. 2**j** shows the Raman spectra of NiO and Pd/NiO. Pd does not show peaks in Raman spectrum because pure metals are highly reflective with the presence of free electrons on theirs surface presumably resulting in non-

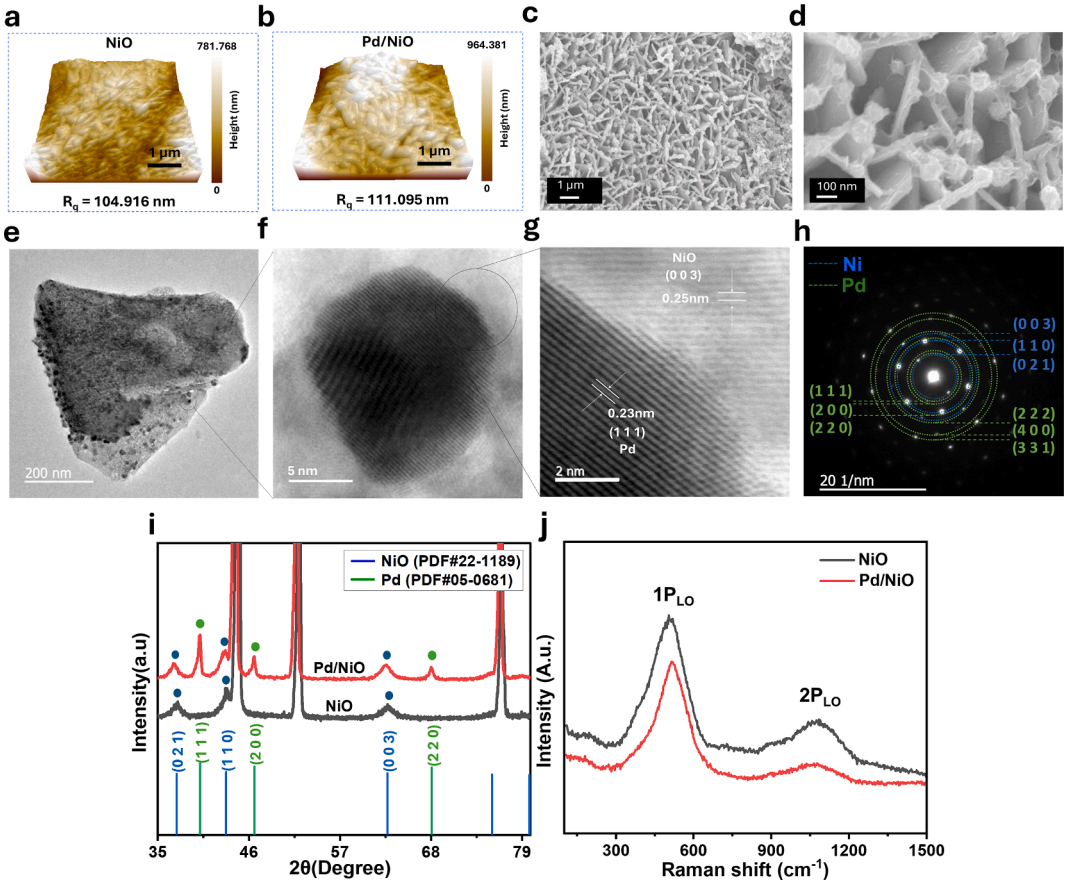

Fig. 2. (a,b) 3D AFM topography images of 5 μm × 5 μm scan area of (a) NiO, and (b) Pd/NiO, (c,d) FE-SEM images of Pd/NiO at different magnifications. (e-g) TEM images of Pd/NiO with various magnifications, (h) corresponding SAED pattern, (i) XRD patterns for NiO and Pd/NiO and (j) Raman spectra of Pd/NiO.

visualized polarizability change of Raman scattering signals [30]. On the other hand, both NiO and Pd/NiO Raman spectra shows two peaks at 530, and 1090 cm^{-1} correspond to one-phonon ($1P_{LO}$) longitudinal optical (LO) and two-phonon ($2P_{LO}$) longitudinal optical of NiO vibrational modes, respectively [31].

X-ray photoelectron spectroscopy (XPS) spectrum was recorded to clarify the surface elemental chemical states and composition of Pd/NiO on the NF substrate (Fig. 3). The XPS survey spectrum displays peaks of Pd, O, and Ni at binding energies of 330–346, 526–540, and 850–890 eV, respectively (Fig. 3**a**).

As shown in Fig. 3**b,** the Pd 3d peaks were separated into Pd $3d_{5/2}$ (335 and 337 eV) and Pd $3d_{3/2}$ (341 and 342 eV) peaks. The intense doublet peaks of 335.9 eV and 340.3 eV correspond to Pd^{2+} (spin orbit energy difference: $\Delta_{BE} = 4.4$ eV) and peak located at 336.6 eV and 342.2 eV imply the existence of Pd^0 ($\Delta_{BE} = 5.6$ eV), indicating the presence of the Pd NPs [32]. Fig. 3**c** shows the deconvoluted O 1s spectra, where the main peak at 529.4 eV is assigned to nickel and oxygen bonding, while the peak at 530.9 eV is ascribed to oxygen in the hydroxide groups [33,34]. The peak at 533 eV indicates adsorbed water on the surface of the sample [35]. The Ni 2p spectrum in Fig. 3**d** reveals two peaks split by spin-orbital coupling: the Ni $2p_{3/2}$ and the Ni $2p_{1/2}$ and corresponding satellite peak (Sat.) located at 860.5 eV and 878.9 eV [36]. In detail, the Ni $2p_{3/2}$ peak was separated into two peaks at 853.3 and 855.1 eV, and Ni $2p_{1/2}$ was divided by two corresponded peaks at 871.2 eV and 872.9 eV corresponding to Ni^{+2} ($\Delta_{BE} = 17.9$ eV), and Ni^{+3} ($\Delta_{BE} = 17.8$ eV), respectively [37]. Various morphological and structural analyses demonstrated the successful fabrication of the Pd-NPs decorated NiO nanostructures on the NF substrates.

2.3. Electrocatalytic performances

The electrocatalytic behavior was characterized by using the Pd-decorated NiO nanostructured electrode as the working electrode, a platinum plate as the counter electrode, and mercury/mercury oxide (Hg/HgO) as the reference electrode in 1.0 M KOH electrolyte. The NiO nanostructures were decorated with different pristine noble metals (Ag, Ru, Au, and Pd) using the same process, that is, alkali-free hydrothermal synthesis followed by wet impregnation, to compare the electrocatalytic effect of each pristine noble metal.

The HER performance of NiO decorated with various pristine noble metals was compared to that of undecorated NiO electrodes to clarify efficiency differences, as shown in Fig. 4.

The electrocatalytic performance of the synthesized electrodes was initially studied through linear sweep voltammetry (LSV) at a scan rate of 2 mV/s, as shown in Fig. 4**a and b**. Comparison of the η_{HER} at 50 and 100 mA cm^{-2} of NiO (230 and 269 mV), Ag/NiO (227 and 266 mV), Ru/NiO (220 and 256 mV), and Au/NiO (196 and 240 mV) showed that Pd/NiO exhibited an impressive η_{HER} of 59 and 92 mV, respectively. The LSV curves of Pd/NiO showed a redox peak at a potential of 0.05 V vs. RHE (reversible hydrogen electrode), which is close to the ideal potential of the HER (0 V vs. RHE). This phenomenon is perhaps attributed to the higher performance of Pd compared to that of the other pristine noble metals [38].

Fig. 4**c** shows the electrochemical impedance spectroscopy (EIS) plots (Nyquist plots) of the electrocatalysts. Note that the increased conductivity of the electrode arises from the lower electrode resistance (R_s) defined in the Z' vertical line. The R_s value of NiO was much higher than that of NiO decorated with other pristine noble metals, indicating the lower conductivity of NiO due to the absence of pristine metal. The low charge transfer resistance (R_{ct}) predicted by the shape of the EIS curve indicates the resistance of the electrolytes in the diffusive area near the electrode interface. The EIS curve parallel to the Y-axis indicates faster ion transfer to the electrode/electrolyte interface in the HER. The smallest R_s and R_{ct} values for Pd/NiO suggest both high conductivity and fast charge transfer, which can enhance the HER.

The kinetics of the HER can be estimated from the relationship between the η_{HER}, and their corresponding logarithm of the current density based on the LSV plots. The mentioned relationship converted slope (Tafel slope), indicates the energy required to achieve an active state and vice versa during the HER. Thus, the electrode displayed a lower Tafel slope, indicating improved electrocatalytic activity [35]. Accordingly, Fig. 4**d**, the lowest Tafel slope of 52 mV dec^{-1} was obtained for

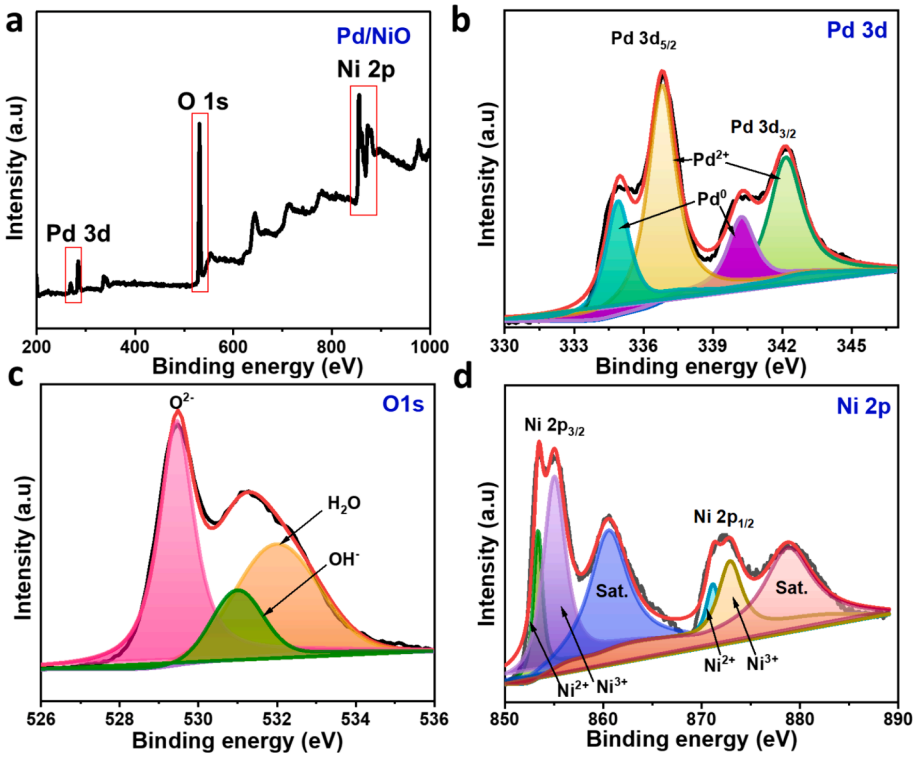

Fig. 3. XPS survey spectrum of (a) Pd/NiO, and high-resolution XPS spectra of (b) Pd 3d, (c) O 1s, and (d) Ni 2p.

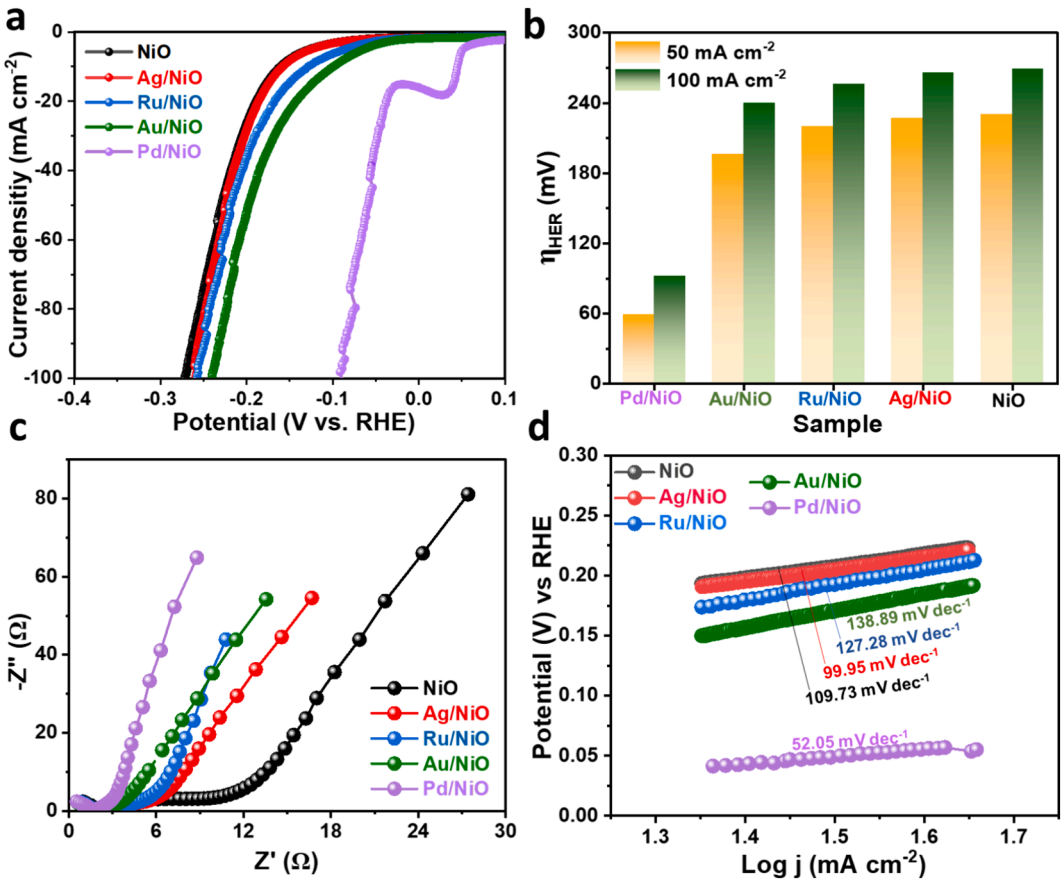

Fig. 4. (a) Linear sweep voltammetry (LSV) curves for the HER over NiO decorated with various pristine noble metals (Ag, Ru, Au, and Pd) in 1.0 M KOH solution at a low scan rate of 2 mV/s^{-1}, (b) overpotential of HER (η_{HER}) at current density of 50 and 100 mA cm^{-2}, (c) electrochemical impedance spectra (EIS) and (d) Tafel slopes of NiO decorated with various pristine noble metals.

Pd/NiO. This value is lower than that of NiO (109 mV dec^{-1}), Ag/NiO (99 mV dec^{-1}), Ru/NiO (127 mV dec^{-1}), and Au/NiO (138 mV dec^{-1}), proving the fast HER kinetics of Pd/NiO. Thus, further detailed studies were conducted to optimize the Pd concentration in the Pd/NiO electrocatalyst to maximize the HER activity.

In the wet impregnation process, concentrations of $PdCl_2$ in the range of 1–5 mM were used to optimize the HER performance. LSV curves were acquired at a scan rate of 2 mV/s for NiO, Pd 1/NiO, Pd 2/NiO, Pd 2.5/NiO, Pd 3/NiO, Pd 3.5/NiO, Pd 4/NiO, and Pd 5/NiO (Fig. 5**a and S5**) electrocatalysts. As mentioned above, the redox peak of the Pd NPs was significantly enhanced at a potential of 0.05 V vs. RHE; however, the LSV curves of NiO and Pd 1/NiO almost overlapped with the η_{HER} of NiO (230 and 269 mV) and Pd 1/NiO (227 and 266 mV) at current densities of 50 mA cm^{-2} and 100 mA cm^{-2}, respectively, indicating lower efficiency at low Pd concentrations. With increasing Pd concentration, Pd 2/NiO (220 and 256 mV) and Pd 2.5/NiO (196 and 240 mV) exhibited lower η_{HER}, but the small redox peaks showing enhanced performance. All remaining samples displayed clear redox peaks in the LSV curves. The redox peak was largest for Pd 3/NiO, which had the lowest η_{HER} of 59 and 92 mV at 50 mA cm^{-2} and 100 mA cm^{-2}, respectively, as shown in Fig. 5**b**. Fig. S5 shows the η_{HER} at 50 mA cm^{-2} and 100 mA cm^{-2} for Pd 3.5/NiO (70 and 123 mV, respectively), Pd 4/NiO (78 and 148 mV, respectively), and Pd 5/NiO (91 and 164 mV, respectively), displaying that the electrocatalytic properties declined as the ratio of Pd NPs in Pd/NiO increased. This phenomenon was presumably due to the occlusion of the NiO nanopores by the aggregated Pd NPs. For further confirmation, the lowest Tafel slope of 52 mV per decade was obtained for Pd 3/NiO in comparison with those of NiO (109 mV dec^{-1}), Pd 1/NiO (99 mV dec^{-1}), Pd 2/NiO (127 mV dec^{-1}), and Pd 2.5/NiO (138 mV dec^{-1}), as shown in Fig. 5d, demonstrating the slowest kinetics for the HER. The EIS profiles of the different Pd-loaded NiO electrocatalysts are shown in Fig. 5**c**. The lowest R_s was observed for Pd 3/NiO (1.62 Ω) as charge transfer occurred more rapidly in this sample than in NiO (1.95 Ω), Pd 1/NiO (1.86 Ω), Pd 2/NiO (1.72 Ω), and Pd 2.5/NiO (1.65 Ω). These results demonstrate that the optimal concentration of Pd in the wet-impregnation step for achieving the highest HER performance was 3 mM. The optimal sample was denoted as Pd/NiO and the LSV test using 1.0 M KOH electrolyte at low scan rate of 2 mVs^{-1} was repeated 10 times as shown in Fig. 4**a** and **Fig. S6**, respectively. It is observed that two samples displayed the same overpotential at −100 mV vs. RHE presumably due to the randomly decorated Pd formed by wet impregnation.

The turnover frequency (TOF) is an intuitive marker of the intrinsic activity of electrocatalysts. The TOF indicates the efficiency as it measures the amount of product formed per unit time for a given amount of electrocatalyst [39]. To analyze the intrinsic electrocatalytic performance of Pd/NiO, the TOF was calculated from the CV curves (**Fig. S7**). The TOF of NiO and Pd/NiO at η_{HER} of −500 mV was estimated as 0.11679 s^{-1} and 0.19954 s^{-1}, respectively, indicating the superior HER performance of Pd/NiO. The electrochemical surface area (ECSA) is one indicator of the intrinsic electrocatalytic activity, as it measures the current divided by the surface area of the catalyst [40]. In principle, the Randles-Sevcik equation involved the redox peaks and the double-layer capacitance (C_{dl}) based on the non-Faradaic area of CV curves in different scan rates can be utilized for ECSA (**Fig. S8a and d**) [41–43]. The minor difference in the C_{dl} of NiO (0.0476 mF cm^{-2}) and Pd/NiO (0.0482 mF cm^{-2}) is attributed to the small difference in the ECSA (1.19 cm^2 (NiO) and 1.22 cm^2 (Pd/NiO)) (**Fig. S8b and e**), presumably due to fewer morphological changes by Pd decoration. Moreover, the charge

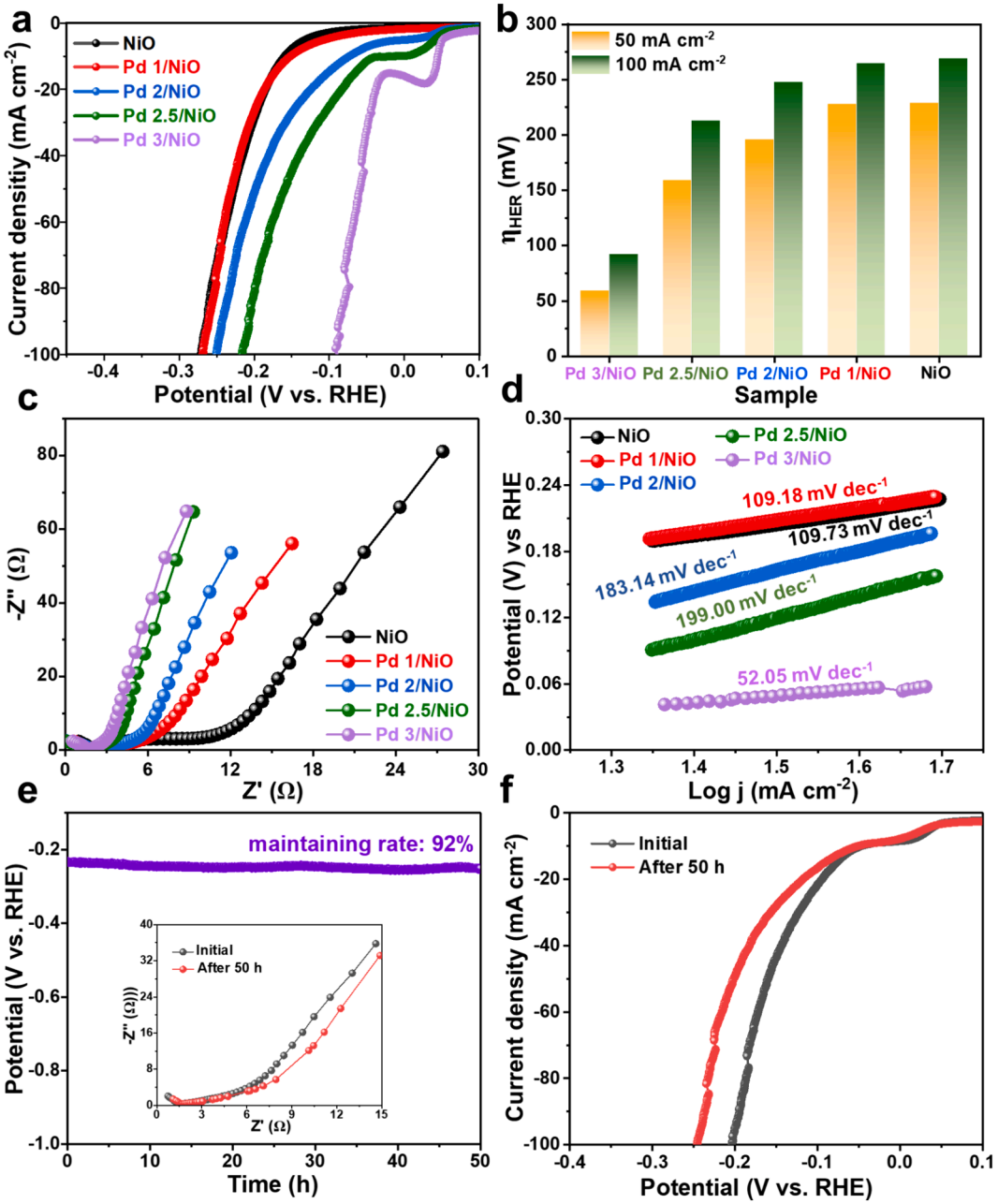

Fig. 5. (a) LSV measurements for various electrocatalysts in HER in 1.0 M KOH solution at a scan rate of 2 mV s^{-1}; (b) η_{HER} at current density of 50 and 100 mA cm^{-2}; (c) EIS curves; and (d) Tafel slopes of various electrocatalysts; (e) stability test by chronopotentiometry at −100 mA cm^{-2} after 50 h (inset shows EIS: initial and after 50 h); (f) LSV curves (iR corrected) for initial state and after 50 h stability test of Pd/NiO.

transfer coefficient is a crucial parameter that reflects the rate of an electrochemical reaction [44]. The charge transfer coefficient can be calculated using Laviron's equations by analyzing the relationship between the logarithm of the scan rate and the logarithm of the potential in CV curves, as shown in **Fig. S8c and f** [45]. The charge transfer coefficient values of NiO and Pd/NiO are 0.73 and 0.58, respectively. The closer charge transfer coefficient value of Pd/NiO to 0.5 compared to that of NiO indicates a more symmetry of energy barrier, meaning that the energy required to transfer the electron is evenly distributed between the reactant and the products [46].

To explore the stability of Pd/NiO, a chronopotentiometry test was conducted over 50 h as shown in Fig. 5**e**. For the long-term testing, the Pt counter electrode was replaced with the graphite rod due to its robustness [59]. The curve remained stable, where 92 % of the initial potential was maintained. The η_{HER} of Pd/NiO did not increase significantly even after 50 h, indicating moderate durability, as confirmed by the corresponding change in the LSV curves (Fig. 5**f**). The FE-SEM image of Pd/NiO after the stability test shows that the nanostructures were maintained (**Fig. S9**). The HER performance of various previously reported electrocatalysts (**Table S1**) and esspecially, Pd-supported electrocatalysts (Table 1) demonstrated the low η_{HER} and Tafel slopes of Pd-supported electrocatalysts; demonstrated the higher HER performance (overpotential at −50/−100 mA cm^{-2} and Tafel slopes) of Pd/NiO compared to that of HER electrocatalysts in previous studies. Moreover, the η_{HER} of Pd/NiO for the HER (92 mV) was approximate with that of commercial Pt/C (88 mV) at 100 mA cm^{-2}.

2.4. First-principles calculations

DFT calculations were performed to investigate the activity of the

Table 1
Comparison of HER activity of various Pd-supported electrocatalysts in 1.0 M KOH electrolyte.

Electrocatalyst	Electrolyte	η_{HER} at −50/−100 mA cm^{-2} (mV)	Tafel slope (mVdec^{-1})	Stability time (h)	Reference
Pd_2RuO_x	1.0 M KOH	49/–	25.6	20	[47]
Pd/ZIS-T	0.5 M H_2SO_4	86/–	33	105	[48]
$Pd_{63}Ni_{16}Fe_{21}$	0.5 M H_2SO_4	170/231	52	24	[49]
np-NiPd/MG	1.0 M KOH	51/213	52.4	20	[50]
PdP_2@CB	1.0 M KOH	120/–	42.1	10	[51]
Pd-NP@MPC-300	1.0 M KOH	60/92	31.1	50	[52]
Pd/N–MoO_2–Mo_2C	1.0 M KOH	102/-	46.1	50	[53]
Pd–Mn_3O_4	0.5 M H_2SO_4	112/193	42	36	[54]
PdSNC	0.5 M H_2SO_4	102/178	56.7	15	[55]
PdCu@Pd NCs	0.5 M H_2SO_4	114/144	35	48	[56]
Pd@MOF-74-Co-3	0.5 M H_2SO_4	254/362	57	–	[57]
Pd0·12/Co@NC	0.5 M H_2SO_4	135/201	42	–	[58]
Pd/NiO	1.0 M KOH	**59/92**	**52**	**50**	**This work**

catalyst and mechanism of the HER on the surfaces of NiO and Pd/NiO. The proposed HER mechanism at the Pd/NiO interface is illustrated in Fig. 6**a**. Initially, H_2O is absorbed. The dissociated OH* and H* are absorbed on the adjacent Pd sites of Pd/NiO. The OH* species gains an electron to form OH^-. Subsequently, the adsorbed H* follows the Heyrovsky–Tafel steps, leading to the formation of H_2. Furthermore, the total density of states (TDOS) and partial density of states (PDOS) of Pd/NiO exhibited continuous distributions near the Fermi level, displaying

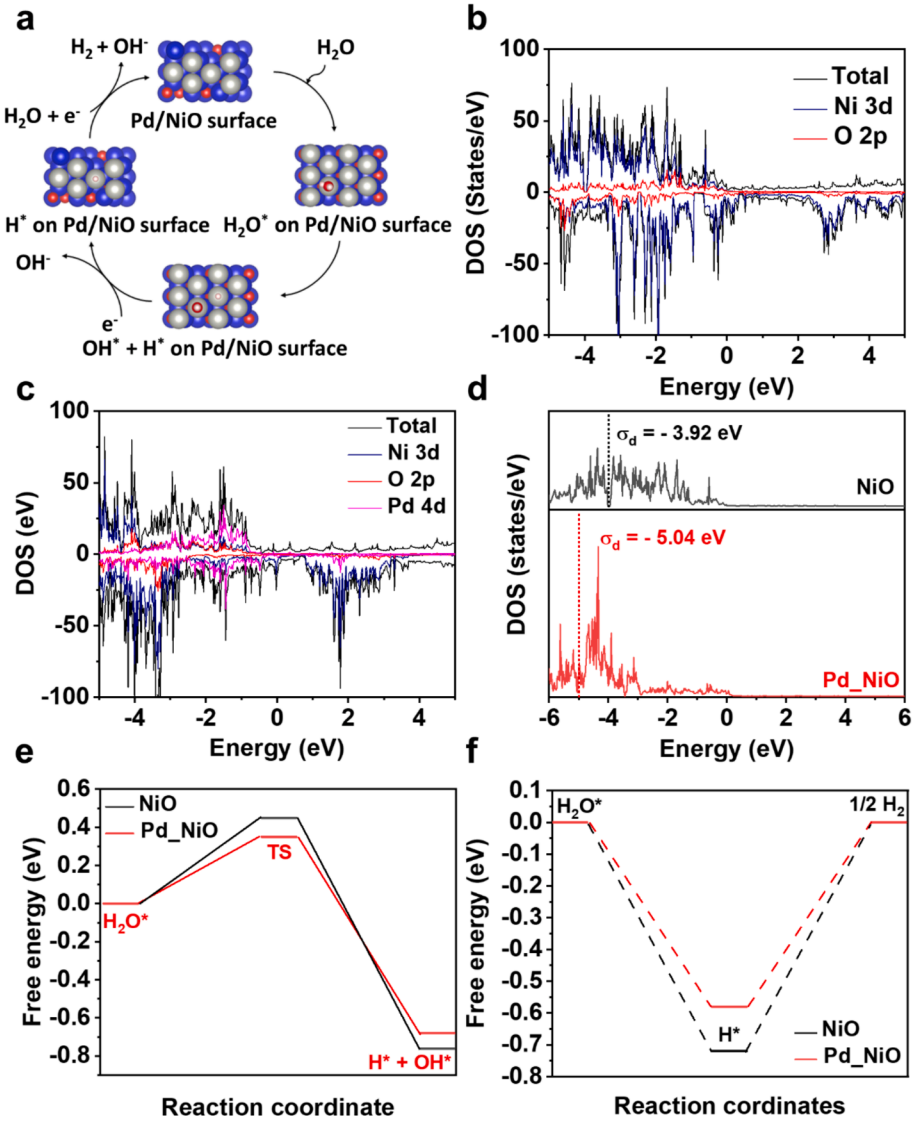

Fig. 6. (a) Proposed mechanism of the HER on the Pd-decorated NiO surface (blue ball: Ni, red ball: O and silver ball: Pd; total DOS of (b) NiO and (c) Pd/NiO; (d) calculated d-band center for NiO and Pd/NiO; (e) Calculated Gibb's free energy in H_2O dissociation step for NiO and Pd/NiO and (f) HER free-energy change from DFT calculation.

that Pd/NiO was in the metallic state with favorable electrical conductivity, which accelerated electron transport during electrocatalysis (Fig. 6**b–d**). The calculated d-band centers for NiO and Pd/NiO are −3.92 and −5.04 eV, respectively. The d-band centers of NiO and Pd/NiO were experimentally determined, indicating a shifted toward lower energy of the d-band center in Pd/NiO (−5.04 eV) compared to that of NiO (−3.92 eV). The creation of the Pd/NiO heterojunction hindered H* adsorption and enhanced the HER activity. Furthermore, the H_2O dissociation energy barriers were calculated for NiO and Pd/NiO, as shown in Fig. 6**e**. Pd/NiO exhibited a lower water dissociation energy barrier (0.35 eV) than NiO (0.46 eV), indicating that H_2O dissociation occurred more easily on the surface of the Pd/NiO catalyst. The Gibbs free energy change for NiO, determined from Fig. 6**f**, was −0.78 eV, suggesting that the Ni sites of NiO act as catalytic centers. The change in the Gibbs free energy for the Pd/NiO heterostructures was approximately −0.52 eV, which is smaller than that of NiO (−0.78 eV). These results indicate that H* adsorption on the Ni and NiO sites was somewhat restricted during the HER but was significantly weakened after the formation of the Pd/NiO heterojunction. Consequently, the Pd sites in the Pd/NiO heterostructure exhibit enhanced adsorption kinetics and HER activity.

3. Experimental section

3.1. Synthesis of Pd/NiO electrocatalyst

The detailed experimental procedures, chemicals, and materials used are shown in Fig. 7. Initially, a piece of 2 cm × 4 cm NF was cleaned using a mixture of H_2SO_4 (acid) and H_2O (water) in a 1:4 ratio in a bath sonication for 1 h to remove the oxide layer on the surface of NF and contaminations. Subsequently, the NF was sonicated for 20 min to eliminate the surface oxide layer, followed by rinsing with deionized (DI) water and immersion in acetone for 20 min to remove the acid residues trapped within the porous structures of the NF. Pristine NiO was synthesized *via* a simple alkali-free *in situ* hydrothermal method. The precursor solution comprising 0.087 g of $Ni(NO_3)_2{\cdot}6H_2O$ was carefully introduced into an 80 mL Teflon-lined hydrothermal reactor. Subsequently, the cleaned NF substrate was submerged in the precursor solution. The hydrothermal reactor was placed inside a stainless-steel autoclave, which was then kept in an electric oven at 180 °C for 6 h. Afterward, the system was cooled, and the NFs were rinsed with DI water to remove the contaminations and annealed at 350 °C for 30 min. To prepare Pd/NiO, a section of the NiO-coated NF was immersed in a 3 mM aqueous solution of Pd ions for 24 h to facilitate the deposition of Pd ions on the NiO surface. Subsequently, the sample was rinsed with DI water to eliminate loosely adsorbed or excess palladium and then dried in an oven at 60 °C for 12 h. Other noble-metal-decorated NiO samples were also prepared using the same process and denoted as Ag/NiO, Ru/NiO, and Au/NiO. Pd/NiO. For optimizing elemental ratios of the Pd/NiO electrode, the samples were prepared with 1; 2; 2.5; 3; 3.5; 4 and 5 mM $PdCl_2$ for the wet impregnation and denoted as Pd 1/NiO, Pd 2/NiO, Pd 2.5/NiO, Pd 3/NiO, Pd 3.5/NiO, Pd 4/NiO, and Pd 5/NiO based on the concentration of Pd^{2+} in the solution. The chemical information and experimental details were described in ***SI1***, and **Table S2** (supporting information), respectively.

3.2. Characterizations

The crystal structure determinations were performed by X-ray diffraction (XRD) using a PANalytical (X'pert PRO) powder diffractometer with a Cu-Kα (λ = 1.54056 Å) radiation source. Raman scattering spectrum was obtained by LabRam Soleil (Horiba) using a single green laser source (550 nm). High-resolution transmission electron microscopy (HR-TEM, JEM-ARM200F) and field-emission scanning electron microscopy (FE-SEM, Carl Zeiss Gemini500) equipped with an energy-dispersive X-ray spectroscopy (EDS) mapping system were used to characterize the morphologies and chemical states of the elements on the electrocatalyst surfaces. A transmission electron microscope (TEM, Hitachi-H 7650) with a magnification in the range of 200–200,000 was used to determine the bulk structure. Atomic force microscopy (AFM, Park NX10) images were obtained the area of 5 μm × 5 μ m and analyzed by the Park System software. The valences of the elements in the compounds were determined by X-ray photoelectron spectroscopy (XPS) analysis (Nexsa XPS, Thermo Fisher Scientific).

3.3. Electrochemical analysis

Electrochemical measurements were invested using an electrochemical workstation (IVIUM nSTAT); the electrochemical assessments were performed at 26 °C. LSV was scanned in the negative potential range of 0 V to −2 V. Nyquist plots were constructed from EIS data obtained with an amplitude of 5 mV in the frequency range of 10^{-4}–100 kHz at the corresponding open-circuit voltage. Chronopotentiometry was performed at −100 mA cm^{-2} over 50 h for the stability test. Because of the leakage of Pt ions in the stability test with the Pt counter electrode, which caused an unintended increase in the HER performance, a stability test was performed with a carbon rod counter electrode. The details calculation in electrochemical analysis were explained in ***SI2*** (supporting information).

3.4. Density functional theory (DFT) experiments

DFT calculations were conducted using the Perdew (Burke) Ernzerhof generalized gradient approximation [60] within the Vienna ab initio simulation package (VASP 6.1.2) code [61]. The forces between the ions and electrons were described using the plane-wave basis set using the projector augmented wave (PAW) method,[62] with electronic eigenfunctions expanded using an energy cutoff of 520 eV. The convergence criteria were set at 1 × 10^{-5} eV for the energy and 0.01 eV/Å as the maximum force during ionic relaxation [63].

4. Conclusion

In this work, Pd NPs-decorated NiO nanoplate electrodes were synthesized by an interfacial engineering approach for application in the HER. The Pd/NiO electrodes successfully grown on the NF substrate by alkali-free hydrothermal synthesis followed by wet impregnation demonstrating excellent HER performance. Remarkable electrocatalytic properties showing the lowest η_{HER} of 59 and 92 mV at current densities of 50 and 100 mA cm^{-2}, respectively, and 92 % efficiency maintained after 50 h of a stability test were achieved by optimizing the composition

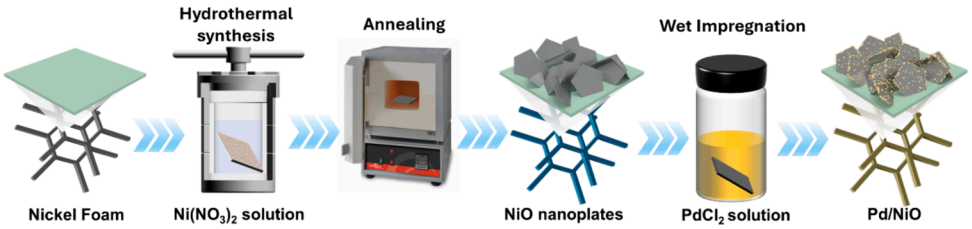

Fig. 7. The schematic of Pd/NiO fabrication by hydrothermal synthesis and subsequent wet impregnation.

of the composite electrodes. The DFT estimations of the dissociation and Gibbs free energies of the electrocatalysts supported well the experimental results. This approach for synthesizing nanostructured transition metal oxide electrodes decorated with small amounts of noble metals created by interfacial engineering can be further utilized for developing novel and efficient electrocatalysts for the HER application.

CRediT authorship contribution statement

Jeongsik Choi: Writing – original draft, Software, Formal analysis, Conceptualization. **Que Thi Nguyen:** Writing – review & editing, Methodology, Data curation, Conceptualization. **Soojin Park:** Formal analysis. **Balaji G. Ghule:** Software, Formal analysis, Data curation. **Jong Hyun Park:** Visualization. **Jae Ryang Park:** Visualization. **Umesh T. Nakate:** Writing – review & editing, Validation, Supervision, Data curation. **Ji-Hyun Jang:** Validation, Data curation. **Dong-Won Kim:** Validation, Data curation. **Sungjune Park:** Writing – review & editing, Supervision, Project administration, Investigation, Funding acquisition.

Declaration of competing interest

The authors declare that they have no known competing financial interests or personal relationships that could have appeared to influence the work reported in this paper.

Data availability

The data that support the findings of this study are available from the corresponding author upon reasonable request.

Acknowledgments

This work was supported by the National Research Foundation of Korea (NRF) grant funded by the Korean Government (MSIT) (RS-2024-00335216) and the Korea Environmental Industry & Technology Institute (KEITI) through the Development of Recycling Promotion Technology for Future Waste Resources Program, funded by the Korea Ministry of Environment (MOE) (RS-2022-KE002082). The authors thank the Center for University-wide Research Facilities, JBNU, for XRD, TEM and FE–SEM collection. The authors thank KBSI Jeonju–si for XPS and HR-TEM analysis. The authors also thank to SKKU equipment sharing system (SESS) for AFM and Raman spectroscopy analysis and UNIST supercomputing center for providing the computational support.

Appendix A. Supplementary material

Supplementary data to this article can be found online at https://doi.org/10.1016/j.cej.2024.154407.

References

[1] I. Roger, M.A. Shipman, M.D. Symes, Earth-abundant catalysts for electrochemical and photoelectrochemical water splitting, Nat. Rev. Chem. 11 (1) (2017) 1–13, https://doi.org/10.1038/s41570-016-0003.
[2] C. Wei, R.R. Rao, J. Peng, B. Huang, I.E.L. Stephens, M. Risch, Z.J. Xu, Y. Shao-Horn, Recommended practices and benchmark activity for hydrogen and oxygen electrocatalysis in water splitting and fuel cells, Adv. Mater. 31 (2019), https://doi.org/10.1002/ADMA.201806296.
[3] L. Su, D. Gong, Y. Jin, D. Wu, W. Luo, Recent advances in alkaline hydrogen oxidation reaction, J. Energy Chem. 66 (2022) 107–122, https://doi.org/10.1016/J.JECHEM.2021.07.015.
[4] X. Jia, W. An, Adsorption of monocyclic aromatics on transition metal surfaces: insight into variation of binding strength from first-principles, J. Phys. Chem. C 122 (2018) 21897–21909, https://doi.org/10.1021/acs.jpcc.8b06321.
[5] J. Yu, Y. Dai, Q. He, D. Zhao, Z. Shao, M. Ni, A mini-review of noble-metal-free electrocatalysts for overall water splitting in non-alkaline electrolytes, Mater. Reports Energy 1 (2021) 100024, https://doi.org/10.1016/j.matre.2021.100024.
[6] L. Zhang, Q. Fan, K. Li, S. Zhang, X. Ma, First-row transition metal oxide oxygen evolution electrocatalysts: regulation strategies and mechanistic understandings, Sustain Energy Fuels 4 (2020) 5417–5432, https://doi.org/10.1039/D0SE01087A.
[7] T. Zhang, M.Y. Wu, D.Y. Yan, J. Mao, H. Liu, W. Bin Hu, X.W. Du, T. Ling, S. Z. Qiao, Engineering oxygen vacancy on NiO nanorod arrays for alkaline hydrogen evolution, Nano Energy 43 (2018) 103–109, https://doi.org/10.1016/j.nanoen.2017.11.015.
[8] V. Manjunath, S. Bimli, R. Biswas, P.N. Didwal, K.K. Haldar, M. Mahajan, N. G. Deshpande, P.A. Bhobe, R.S. Devan, Experimental investigations on morphology controlled bifunctional NiO nano-electrocatalysts for oxygen and hydrogen evolution, Int. J. Hydrogen Energy 47 (2022) 39018–39029, https://doi.org/10.1016/j.ijhydene.2022.09.054.
[9] Q. Wang, G. Wang, J. Wang, J. Li, K. Wang, S. Zhou, Y. Su, In Situ Hydrothermal synthesis of ZnS/TiO2 nanofibers S-scheme heterojunction for enhanced photocatalytic H2 evolution, Adv. Sustain. Syst. 7 (2023), https://doi.org/10.1002/ADSU.202200027.
[10] A. Sobhani, M. Salavati-Niasari, Transition metal selenides and diselenides: Hydrothermal fabrication, investigation of morphology, particle size and and their applications in photocatalyst, Adv. Colloid Interface Sci. 287 (2021) 102321, https://doi.org/10.1016/j.cis.2020.102321.
[11] K. Xu, L. Wang, S. Xiong, C. Ge, L. Wang, B. Wang, W. Wang, M. Chen, G. Liu, Hydrothermally prepared ultra-stable multilayer nanoflake NiO-based electrochromic films, Electrochim. Acta 441 (2023) 141812, https://doi.org/10.1016/J.ELECTACTA.2022.141812.
[12] B. Mehrabi Matin, Y. Mortazavi, A.A. Khodadadi, A. Abbasi, A. Anaraki Firooz, Alkaline- and template-free hydrothermal synthesis of stable SnO2 nanoparticles and nanorods for CO and ethanol gas sensing, Sensors Actuators B Chem. 151 (2010) 140–145, https://doi.org/10.1016/j.snb.2010.09.033.
[13] Q.T. Nguyen, U.T. Nakate, J. Chen, S. Park, S. Park, Ceria nanoflowers decorated Co3O4 nanosheets electrodes for highly efficient electrochemical supercapacitors, Appl. Surf. Sci. 613 (2023) 156034, https://doi.org/10.1016/j.apsusc.2022.156034.
[14] F. Song, L. Bai, A. Moysiadou, S. Lee, C. Hu, L. Liardet, X. Hu, Transition metal oxides as electrocatalysts for the oxygen evolution reaction in alkaline solutions: an application-inspired renaissance, J. Am. Chem. Soc. 140 (2018) 7748–7759, https://doi.org/10.1021/JACS.8B04546/ASSET/IMAGES/LARGE/JA-2018-04546Q_0006.JPEG.
[15] S. Gong, Y.X. Zhang, Z. Niu, Recent advances in earth-abundant core/noble-metal shell nanoparticles for electrocatalysis, ACS Catal. 10 (2020), https://doi.org/10.1021/acscatal.0c02587.
[16] Z.Q. Liu, H. Cheng, N. Li, T.Y. Ma, Y.Z. Su, ZnCo2O4Quantum dots anchored on nitrogen-doped carbon nanotubes as reversible oxygen reduction/evolution electrocatalysts, Adv. Mater. 28 (2016) 3777–3784, https://doi.org/10.1002/adma.201506197.
[17] J.J. Gao, P. Du, Q.H. Zhang, X. Shen, F.-K. Chiang, Y.R. Wen, X. Lin, X.J. Liu, H. J. Qiu, Platinum single atoms/clusters stabilized in transition metal oxides for enhanced electrocatalysis, Electrochim. Acta 297 (2019) 155–162, https://doi.org/10.1016/j.electacta.2018.11.200.
[18] C. Xie, Z. Niu, D. Kim, M. Li, P. Yang, Surface and interface control in nanoparticle catalysis, Chem. Rev. 120 (2020) 1184–1249, https://doi.org/10.1021/acs.chemrev.9b00220.
[19] Y. Li, Y. Sun, Y. Qin, W. Zhang, L. Wang, M. Luo, H. Yang, S. Guo, Recent advances on water-splitting electrocatalysis mediated by noble-metal-based nanostructured materials, Adv. Energy Mater. 10 (2020), https://doi.org/10.1002/aenm.201903120.
[20] Y. Yan, J. Lin, T. Xu, B. Liu, K. Huang, L. Qiao, S. Liu, J. Cao, S.C. Jun, Y. Yamauchi, J. Qi, Atomic-level platinum filling into ni-vacancies of dual-deficient NiO for boosting electrocatalytic hydrogen evolution, Adv. Energy Mater. 12 (2022), https://doi.org/10.1002/aenm.202200434.
[21] L. Zhang, Z. Hu, H. Li, Q. Ren, Y. Qiu, J. Qu, S. Hu, Nickel foam Supported NiO@Ru heterostructure towards high-efficiency overall water splitting, ChemPhysChem 22 (2021) 1785–1791, https://doi.org/10.1002/cphc.202100317.
[22] A. Barhoum, H.H. El-Maghrabi, I. Iatsunskyi, E. Coy, A. Renard, C. Salameh, M. Weber, S. Sayegh, A.A. Nada, S. Roualdes, M. Bechelany, Atomic layer deposition of Pd nanoparticles on self-supported carbon-Ni/NiO-Pd nanofiber electrodes for electrochemical hydrogen and oxygen evolution reactions, J. Colloid Interface Sci. 569 (2020) 286–297, https://doi.org/10.1016/j.jcis.2020.02.063.
[23] S. Ghasemi, S.R. Hosseini, S. Nabipour, P. Asen, Palladium nanoparticles supported on graphene as an efficient electrocatalyst for hydrogen evolution reaction, Int. J. Hydrogen Energy 40 (2015) 16184–16191, https://doi.org/10.1016/j.ijhydene.2015.09.114.
[24] S. Sarkar, S.C. Peter, An overview on Pd-based electrocatalysts for the hydrogen evolution reaction, Inorg. Chem. Front. 5 (2018) 2060–2080, https://doi.org/10.1039/c8qi00042e.
[25] A.F. Suzana, L. Wu, T.A. Assefa, B.P. Williams, R. Harder, W. Cha, C.-H. Kuo, C.-K. Tsung, I.K. Robinson, Structure of a seeded palladium nanoparticle and its dynamics during the hydride phase transformation, Commun. Chem. 4 (2021) 64, https://doi.org/10.1038/s42004-021-00500-7.
[26] P. Chakraborty, N. Deka, D.C. Patra, K. Debnath, S.P. Mondal, Salivary glucose sensing using highly sensitive and selective non-enzymatic porous NiO nanostructured electrodes, Surfaces Interfaces 26 (2021) 101324, https://doi.org/10.1016/j.surfin.2021.101324.
[27] D. Su, M. Ford, G. Wang, Mesoporous NiO crystals with dominantly exposed 110 reactive facets for ultrafast lithium storage, Sci. Rep. 2 (2012) 1–7, https://doi.org/10.1038/srep00924.
[28] K. Qi, W. Zheng, X. Cui, Supersaturation-controlled surface structure evolution of Pd@Pt core-shell nanocrystals: Enhancement of the ORR activity at a sub-10 nm scale, Nanoscale 8 (2016) 1698–1703, https://doi.org/10.1039/c5nr07940c.

[29] Y. Xiong, J.M. McLellan, Y. Yin, Y. Xia, Synthesis of palladium icosahedra with twinned structure by blocking oxidative etching with citric acid or citrate ions, Angew. Chemie - Int. Ed. 46 (2007) 790–794, https://doi.org/10.1002/anie.200604032.
[30] R. Carles, M. Bayle, P. Benzo, G. Benassayag, C. Bonafos, G. Cacciato, V. Privitera, Plasmon-resonant Raman spectroscopy in metallic nanoparticles: Surface-enhanced scattering by electronic excitations, Phys. Rev. B - Condens. Matter Mater. Phys. 92 (2015), https://doi.org/10.1103/PhysRevB.92.174302.
[31] A.Y. Faid, A.O. Barnett, F. Seland, S. Sunde, Ni/NiO nanosheets for alkaline hydrogen evolution reaction: In situ electrochemical-Raman study, Electrochim. Acta 361 (2020) 137040, https://doi.org/10.1016/j.electacta.2020.137040.
[32] P. Wu, Y. Huang, L. Kang, M. Wu, Y. Wang, Multisource synergistic electrocatalytic oxidation effect of strongly coupled PdM (M=Sn, Pb)/N-doped graphene nanocomposite on small organic molecules, Sci. Rep. 5 (2015) 1–10, https://doi.org/10.1038/srep14173.
[33] Y. Wang, X. Yang, J. Yu, A polysalen based on polyacylamide stabilized palladium nanoparticle catalyst for efficient carbonylative Sonogashira reaction in aqueous media, RSC Adv. 7 (2017) 31850–31857, https://doi.org/10.1039/c7ra04910b.
[34] T. Zhou, Z. Cao, P. Zhang, H. Ma, Z. Gao, H. Wang, Y. Lu, J. He, Transition metal ions regulated oxygen evolution reaction performance of Ni-based hydroxides hierarchical nanoarrays, Nat. Publ. Gr. (2017) 1–9, https://doi.org/10.1038/srep46154.
[35] A. Sivanantham, P. Ganesan, S. Shanmugam, Hierarchical NiCo2S4 nanowire arrays supported on Ni foam: an efficient and durable bifunctional electrocatalyst for oxygen and hydrogen evolution reactions, Adv. Funct. Mater. 26 (2016) 4661–4672, https://doi.org/10.1002/adfm.201600566.
[36] C. Wu, S. Deng, H. Wang, Y. Sun, J. Liu, H. Yan, Preparation of novel three-dimensional NiO/ultrathin derived graphene hybrid for supercapacitor applications, ACS Appl. Mater. Interfaces 6 (2014) 1106–1112, https://doi.org/10.1021/am404691w.
[37] G.H. Yu, F.W. Zhu, C.L. Chai, X-ray photoelectron spectroscopy study of magnetic films, Appl. Phys. A Mater. Sci. Process. 76 (2003) 45–47, https://doi.org/10.1007/s003390201292.
[38] M. Chen, S.M. Lu, Y.Y. Peng, Z. Ding, Y.T. Long, Tracking the Electrocatalytic activity of a single palladium nanoparticle for the hydrogen evolution reaction, Chem. - A Eur. J. 27 (2021) 11799–11803, https://doi.org/10.1002/chem.202101263.
[39] S. Anantharaj, P.E. Karthik, S. Noda, The significance of properly reporting turnover frequency in electrocatalysis research, Angew. Chemie - Int. Ed. 60 (2021) 23051–23067, https://doi.org/10.1002/anie.202110352.
[40] C. Wei, S. Sun, D. Mandler, X. Wang, S.Z. Qiao, Z.J. Xu, Approaches for measuring the surface areas of metal oxide electrocatalysts for determining their intrinsic electrocatalytic activity, Chem. Soc. Rev. 48 (2019) 2518–2534, https://doi.org/10.1039/c8cs00848e.
[41] K.V. Mounesh, A. Yatish, G.E. Pandith, B.M. Eldesoky, Nagaraja, A novel MWCNT-encapsulated (2-aminoethyl)piperazine-decorated zinc(<scp>ii</scp>) phthalocyanine composite: development of an electrochemical sensor for detecting the antipsychotic drug promazine in environmental samples, J. Mater. Chem. B 11 (2023) 10692–10705, https://doi.org/10.1039/D3TB01859H.
[42] P. Mounesh, R.R. Manikanta, G. Nikam, B.M. Tigari, Nagaraja, Novel nickel (<scp>ii</scp>) phthalocyanine/reduced graphene oxide: an electrochemical sensing platform for analysis of hydroquinone and chloramphenicol in environmental samples, Anal. Methods 16 (2024) 1770–1784, https://doi.org/10.1039/D4AY00087K.
[43] C.C.L. McCrory, S. Jung, J.C. Peters, T.F. Jaramillo, Benchmarking heterogeneous electrocatalysts for the oxygen evolution reaction, J. Am. Chem. Soc. 135 (2013) 16977–16987, https://doi.org/10.1021/ja407115p.
[44] E. Laviron, The use of linear potential sweep voltammetry and of a.c. voltammetry for the study of the surface electrochemical reaction of strongly adsorbed systems and of redox modified electrodes, J. Electroanal. Chem. 100 (1979) 263–270, https://doi.org/10.1016/S0022-0728(79)80167-9.
[45] P. Manikanta, R.R. Mounesh, S. Nikam, B.M. Sandeep, Nagaraja, Development of novel microsphere structured – calcium tungstate as efficacious electrocatalyst for the detection of antibiotic drug nitrofurantoin, J. Mater. Chem. B 11 (2023) 11600–11611, https://doi.org/10.1039/D3TB02087H.
[46] C. Costentin, M. Robert, J.M. Savéant, Electron transfer and bond breaking: recent advances, Chem. Phys. 324 (2006) 40–56, https://doi.org/10.1016/j.chemphys.2005.09.029.
[47] V. Do, P. Prabhu, V. Jose, T. Yoshida, Y. Zhou, H. Miwa, T. Kaneko, T. Uruga, Y. Iwasawa, J. Lee, Pd – PdO nanodomains on amorphous ru metallene oxide for high-performance multifunctional, Electrocatalysis (2023) 1–14, https://doi.org/10.1002/adma.202208860.
[48] D. Wang, H. Yang, S. Tian, G. Liu, Y. Wang, X. Sun, Z. Wang, J. Hou, F. Ma, S. Peng, High dispersion Pd nanoclusters modified sulfur-rich vacancies ZnIn2S4 for high-performance hydrogen evolution, Appl. Surf. Sci. 638 (2023) 157926, https://doi.org/10.1016/j.apsusc.2023.157926.
[49] P. Zou, L. Song, W. Xu, M. Gao, V. Zadorozhnyy, J. Huo, J.Q. Wang, High-throughput screening of superior hydrogen evolution reaction catalysts in Pd-Ni-Fe alloys, J. Alloys Compd. 960 (2023) 170656, https://doi.org/10.1016/j.jallcom.2023.170656.
[50] X. Liu, S. Zhu, Y. Liang, H. Jiang, Z. Li, S. Wu, Z. Cui, Self-standing nanoporous NiPd bimetallic electrocatalysts with ultra-low Pd loading for efficient hydrogen evolution reaction, Electrochim. Acta 411 (2022) 140077, https://doi.org/10.1016/j.electacta.2022.140077.
[51] F. Luo, Q. Zhang, X. Yu, S. Xiao, Y. Ling, H. Hu, L. Guo, Z. Yang, L. Huang, W. Cai, H. Cheng, Palladium phosphide as a stable and efficient electrocatalyst for overall water splitting, Angew. Chemie - Int. Ed. 57 (2018) 14862–14867, https://doi.org/10.1002/anie.201810102.
[52] D.S. Butenko, S. Li, V.O. Kotsyubynsky, V.M. Boychuk, V.I. Dubinko, P. I. Kolkovsky, N.A. Liedienov, N.I. Klyui, W. Han, I.V. Zatovsky, Palladium nanoparticles embedded in microporous carbon as electrocatalysts for water splitting in alkaline media, Int. J. Hydrogen Energy 46 (2021) 21462–21474, https://doi.org/10.1016/j.ijhydene.2021.03.242.
[53] L. Karuppasamy, L. Gurusamy, S. Anandan, C.H. Liu, J.J. Wu, Defect-enriched heterointerfaces N-MoO2–Mo2C supported Pd nanocomposite as a novel multifunctional electrocatalyst for oxygen reduction reaction and overall water splitting, Mater. Today Chem. 24 (2022), https://doi.org/10.1016/j.mtchem.2022.100799.
[54] C. Ray, S. Dutta, Y. Negishi, T. Pal, A new stable Pd-Mn3O4 nanocomposite as an efficient electrocatalyst for the hydrogen evolution reaction, Chem. Commun. 52 (2016) 6095–6098, https://doi.org/10.1039/c6cc01642a.
[55] M.H. Naveen, Y. Huang, S. Bisalere Kantharajappa, K.D. Seo, D.S. Park, Y.B. Shim, Enhanced electrocatalytic activities of in situ produced Pd/S/N-doped carbon in oxygen reduction and hydrogen evolution reactions, ACS Appl. Energy Mater. 4 (2021) 575–585, https://doi.org/10.1021/acsaem.0c02461.
[56] J. Li, F. Li, S.X. Guo, J. Zhang, J. Ma, PdCu@Pd Nanocube with Pt-like activity for hydrogen evolution reaction, ACS Appl. Mater. Interfaces 9 (2017) 8151–8160, https://doi.org/10.1021/acsami.7b01241.
[57] F. Zheng, C. Zhang, X. Gao, C. Du, Z. Zhuang, W. Chen, Immobilizing Pd nanoclusters into electronically conductive metal-organic frameworks as bi-functional electrocatalysts for hydrogen evolution and oxygen reduction reactions, Electrochim. Acta 306 (2019) 627–634, https://doi.org/10.1016/j.electacta.2019.03.175.
[58] H. Liu, C. Liu, X. Zong, Y. Wang, Z. Hu, Z. Zhang, Highly uniform Pd nanoparticles supported on Co-metal organic frameworks-derived carbon as HER electrocatalysts, Int. J. Hydrogen Energy 48 (2023) 31152–31160, https://doi.org/10.1016/j.ijhydene.2023.04.150.
[59] J. Chen, U.T. Nakate, Q.T. Nguyen, S. Park, Electrodeposited Bi(OH)3@Mo(OH)4 nanostructured electrode for high-performance supercapacitor application, Ceram. Int. 48 (2022) 22417–22425, https://doi.org/10.1016/j.ceramint.2022.04.254.
[60] D. Joubert, From ultrasoft pseudopotentials to the projector augmented-wave method, Phys. Rev. B - Condens. Matter Mater. Phys. 59 (1999) 1758–1775, https://doi.org/10.1103/PhysRevB.59.1758.
[61] R.A. Vargas-Hernández, Bayesian optimization for calibrating and selecting hybrid-density functional models, J. Phys. Chem. A 124 (2020) 4053–4061, https://doi.org/10.1021/acs.jpca.0c01375.
[62] L. Wang, T. Maxisch, G. Ceder, Oxidation energies of transition metal oxides within the GGA+U framework, Phys. Rev. B - Condens. Matter Mater. Phys. 73 (2006) 1–6, https://doi.org/10.1103/PhysRevB.73.195107.
[63] X. Yi, X. He, F. Yin, G. Li, Z. Li, Surface strain engineered Ni-NiO for boosting hydrogen evolution reaction in alkaline media, Electrochim. Acta 391 (2021) 138985, https://doi.org/10.1016/j.electacta.2021.138985.